



Ice amplifies ligand-controlled mineral dissolution in microscale hot spots

Tao Chen^a , Tao Luo^a , Tra My Bui Thi^b , Hervé Colloc^b, Claire Roiland^b , Laurent Le Pollès^b, Khalil Hanna^b , and Jean-François Boily^{a,1}

Affiliations are included on p. 7.

Edited by François M. M. Morel, Princeton University, Princeton, NJ; received November 11, 2025; accepted March 25, 2026

Cold-region ecosystems are highly sensitive to climate change, yet the geochemical processes shaping their future remain poorly understood. Here, we show that ice systematically enhances mineral dissolution through freeze concentration into microscale reactive hot spots. Using goethite nanoparticles as a model iron oxide and environmentally relevant inorganic anions common in soils, waters, and aerosols (chloride, fluoride, sulfate), we demonstrate that ligand-promoted dissolution rates under mildly acidic conditions scale with binding affinity in both ice and liquid water, with ice enhancing rates across all reactive ligands. Fluoride, the strongest complexing agent, increased dissolution more than fourfold in ice, while weakly binding perchlorate produced no measurable dissolution in either phase. Reactions persisted well below the eutectic temperature, mediated by minute volumes of liquid-like water stabilized within networks of micron-sized mineral aggregates. Our findings highlight ice as a dynamic medium driving iron release, with implications for nutrient availability, carbon cycling, and biogeochemical feedbacks in rapidly warming polar and alpine regions.

ice | goethite | dissolution | iron | interfaces

Global warming fundamentally alters iron biogeochemical cycling in cold environments through ice shelf melting, declining snow cover, and northward permafrost migration (1, 2). Accumulating reports document iron release to arctic rivers (3), iron-driven carbon mobilization (4), hazardous microbe blooms (5, 6), and greenhouse gas emissions (7). These observations raise critical questions about the underlying geochemical pathways (8, 9). Yet while iron mobilization driven by liquid water from melting ice is relatively well characterized, reactions occurring within the ice matrix itself remain poorly understood. Part of this shortcoming stems from the misconception outside the specialized literature that ice is an inert medium (10).

However, a growing body of literature is demonstrating the important roles that ice plays in the dissolution of minerals of the iron oxide family (Fig. 1) (11–13). This reactivity can be understood by the presence of minute volumes of liquid water within the polycrystalline matrix of ice at temperatures above the eutectic (e.g., $-21.1\text{ }^{\circ}\text{C}$ in NaCl-bearing ice) (12–14). At high salt concentrations, ice crystal lattices clearly expel solutes and mineral nanoparticles during freezing, forming well-defined Liquid Intergrain Boundaries (LIBs). Conversely, at low salt concentrations typical of freshwater, liquid water distribution can become more complex, with solutes dispersed in microscopic liquid films and pockets rather than forming clearly delineated boundaries. Both scenarios create concentrated microenvironments that can trigger reactions not observed in bulk liquid water, though through different spatial organizations.

Iron oxide minerals confined within these liquid zones could play critical roles in biogeochemical processes by supplying bioavailable iron through weathering (15), catalyzing phosphorus transformations (16), and controlling organic carbon stabilization (17) and degradation (18). Understanding these ice-mediated processes has profound implications for multiple scientific disciplines, including geochemistry, hydrology, ecology, and climate science. As it challenges fundamental assumptions about mineral reactivity in frozen systems, it may also require revision of biogeochemical models for cold regions. Current biogeochemical models assume minimal mineral–water interactions at subfreezing temperatures, potentially underestimating nutrient fluxes, trace element cycling, and weathering rates in polar and alpine environments. This knowledge gap becomes increasingly critical as climate change alters the global distribution and stability of frozen systems, affecting $\sim 17\%$ of Earth's land surface underlain by permafrost and vast areas of seasonal ice cover (19).

This study used goethite, a geochemically and atmospherically representative mineral of the iron oxide family, to investigate how inorganic anions affect dissolution reactions

Significance

This study challenges the assumption that ice is geochemically inert, revealing it as a dynamic reactor that accelerates iron oxide dissolution through microscale liquid water networks. The finding that common environmental anions enhance mineral weathering rates in ice has profound implications for understanding biogeochemical processes in Earth's extensive frozen regions. As climate change rapidly alters polar and alpine environments affecting 17% of Earth's permafrost-underlain surface, these findings suggest current models could underestimate nutrient mobilization, trace element cycling, and weathering rates in cold regions. This enhanced iron release mechanism helps explain observed increases in arctic river iron fluxes, carbon mobilization, and greenhouse gas emissions, providing critical insights for predicting biogeochemical feedbacks in our warming world.

Author contributions: T.C., K.H., and J.-F.B. designed research; T.C., T.L., T.M.B.T., H.C., C.R., L.L.P., and K.H. performed research; T.C., T.L., T.M.B.T., H.C., C.R., L.L.P., and J.-F.B. analyzed data; and T.C. and J.-F.B. wrote the paper.

The authors declare no competing interest.

This article is a PNAS Direct Submission.

Copyright © 2026 the Author(s). Published by PNAS. This article is distributed under [Creative Commons Attribution-NonCommercial-NoDerivatives License 4.0 \(CC BY-NC-ND\)](https://creativecommons.org/licenses/by-nc-nd/4.0/).

¹To whom correspondence may be addressed. Email: jean-francois.boily@umu.se.

This article contains supporting information online at <https://www.pnas.org/lookup/suppl/doi:10.1073/pnas.2532599123/-/DCSupplemental>.

Published April 22, 2026.

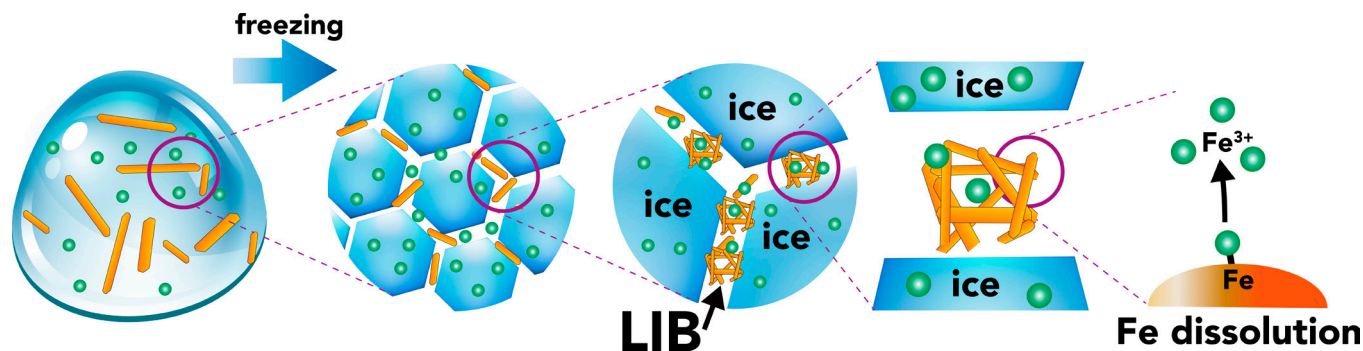


Fig. 1. Schematic representation of freeze concentration effects on iron oxide dissolution in ice. During freezing, mineral nanoparticles (orange rods) and dissolved anions (green circles) are expelled from the ice crystal lattice and concentrated into the liquid intergrain boundary (LIB). This process creates microenvironments with significantly elevated reactant concentrations compared to the initial solution. Enhanced surface complexation between concentrated ligands and mineral surfaces within these confined liquid zones drives accelerated iron dissolution, releasing Fe^{3+} species into solution. The schematic illustrates the fundamental mechanism by which ice functions as a geochemical reactor, transforming dilute mineral suspensions into reactive hot spots that sustain mineral–water interfacial processes at subzero temperatures.

in ice (20). We selected anions with varying iron binding strengths from diverse environmental sources, including chloride (marine environments), fluoride (weathering, atmospheric processes), perchlorate (atmospheric deposition, Mars surface processes), and sulfate (natural waters, acid precipitation). This study builds upon our previous work with oxalate (11), which demonstrated enhanced goethite dissolution in ice through formation of clearly defined LIBs. However, the present study examines low salt conditions, raising the question of the nature of the liquid microenvironments sustaining mineral dissolution reactions in ice. Fluoride served as the primary experimental focus as a strong iron-complexing ligand, enabling detailed mechanistic investigation of surface processes under the mildly acidic conditions common in cold-region soils and aerosols (21, 22).

Through time-resolved dissolution experiments, surface complexation modeling, and spatial mapping, we demonstrate that freeze concentration creates micron-sized reaction hot spots where ligand-promoted dissolution is systematically enhanced. The enhancement magnitude correlates directly with ligand binding affinity, confirming that ice amplifies surface reactions regardless of ligand identity. These findings reveal that ice functions as a geochemical reactor capable of sustaining and accelerating iron oxide dissolution, providing a thermodynamic framework for predicting mineral reactivity across diverse frozen environments.

Results

Ligand-Promoted Fe Release from Goethite in Ice. To explore the production of soluble ferric iron in ice, we froze dilute aqueous suspensions of goethite ($\alpha\text{-FeOOH}$) nanoparticles with fluoride (Fig. 2 and *SI Appendix*, Fig. S1). All time-resolved experiments at pH 2.8 to 5 (Fig. 2 *A* and *B* and *SI Appendix*, Table S2) showed that fluoride enhanced goethite dissolution rates in ice compared to liquid water. Cumulative dissolution yields were consistently 4.3 ± 0.3 times greater in ice than in liquid water across all conditions (Fig. 2*C*). This enhancement in yield persisted throughout the course of 8-d experiments, regardless of fluoride concentration or pH. Supporting the concept that goethite underwent dissolution in ice, transmission electron microscopy revealed a 22% reduction in particle width after 8 continual days of reaction in ice (*SI Appendix*, Fig. S2). X-ray diffraction also showed extensive structural disorder (*SI Appendix*, Fig. S3),

reflecting lattice disruption and crystallite size reduction resulting from iron dissolution in ice (23, 24).

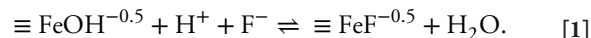
Time-resolved dissolution data exhibited zero-order kinetics in both phases, with total rates (R_T) scaling with decreasing pH and increasing NH_4F concentrations (Fig. 2 *D* and *E*). Rates also correlated linearly with fluoride surface loadings (Γ_F) determined from adsorption experiments in liquid water (Figs. 2 *E* and *F* and 3*A*). This behavior indicates a surface-controlled mechanism where fluoride-bound iron site detachment controls overall dissolution rates.

These kinetic patterns demonstrate that ice preserves fundamental surface chemical mechanisms while systematically enhancing their efficiency. The consistent zero-order behavior and constant enhancement factors across conditions show that mineral–water interfacial processes maintain identical thermodynamic relationships in both phases. The direct correlation between dissolution rates and surface fluoride loadings confirms that enhanced reactivity stems from increased ligand adsorption rather than activation of fundamentally different pathways.

Fluoride Precursor Surface Complexes Leading to Dissolution.

To explain the enhanced uptake of fluoride in ice, a surface complexation model was developed from adsorption data in liquid water (Fig. 3*A* and *SI Appendix*, Fig. S4 and Table S1). The model was based on a priori knowledge of the 2D spatial disposition of reactive goethite surface Fe-bound hydroxyls (Fig. 3 *B–D*), derived from the crystal habit of the synthetic goethite nanoparticles (25), surface structural considerations (Fig. 3 *B–D*), and previous spectroscopic work (22, 26). Based on these considerations, the model accounts for reactive OH sites distinguished by their coordination number with underlying Fe atoms. These include singly ($\equiv\text{FeOH}^{-0.5}$; 3.13 nm^{-2}), doubly ($\equiv\text{Fe}_2\text{OH}$; 3.13 nm^{-2}), and triply coordinated ($\equiv\text{Fe}_3\text{O}^{-0.5}$; 5.93 nm^{-2}) sites (*SI Appendix*, Table S1) (21, 22). Ligand exchangeability, forming Fe-anion surface complexes, correlates directly with this coordination environment, with singly coordinated groups being most readily exchanged, and higher coordination sites less so.

The model (*SI Appendix*, Table S1) favored fluoride adsorption through ligand-exchange with singly coordinated sites on dominant goethite faces (22, 26):



Doubly coordinated site involvement

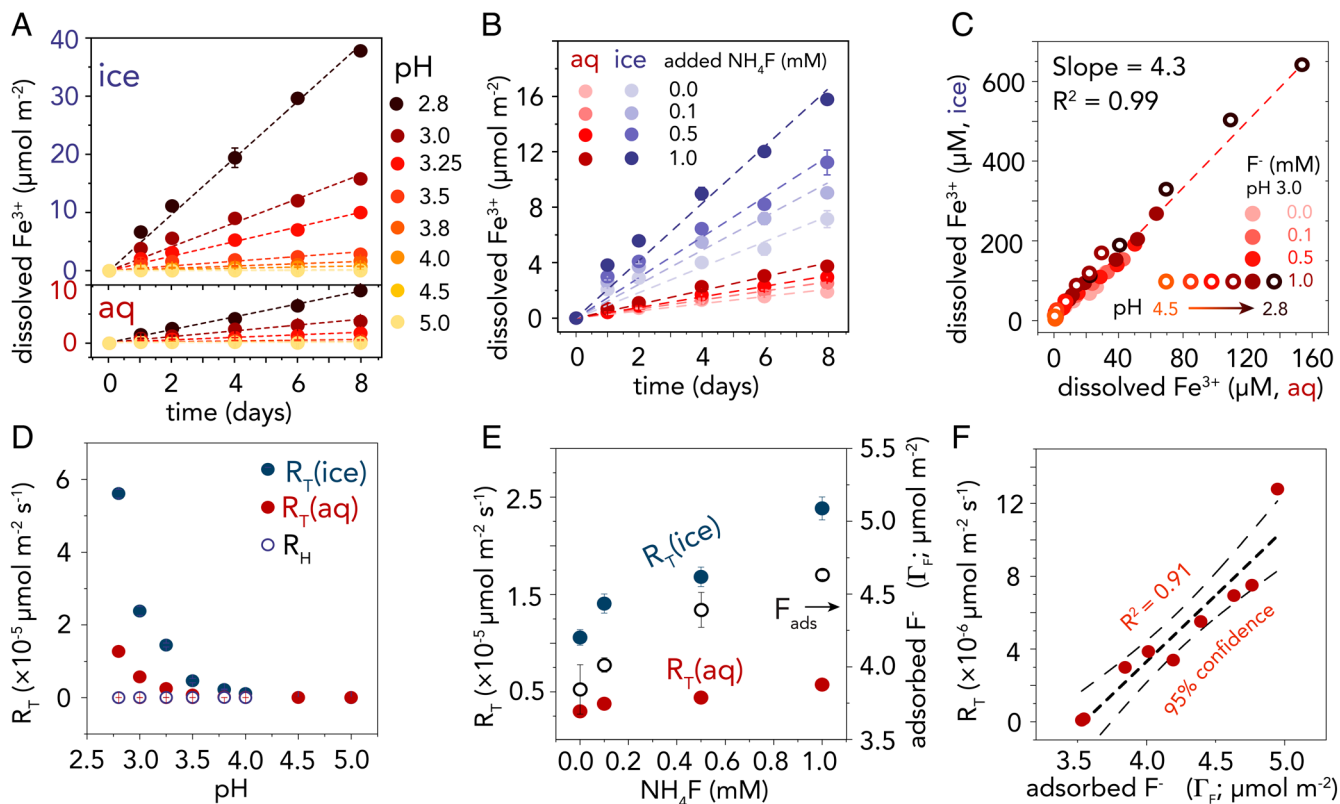
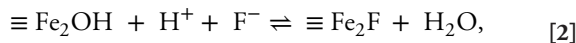


Fig. 2. Fluoride-promoted goethite dissolution correlates with surface complexation and follows thermodynamic control. Time-resolved dissolution of 0.2 g^{-1} goethite in ice ($-20 \text{ }^\circ\text{C}$) vs. liquid water ($25 \text{ }^\circ\text{C}$). (A) pH dependence (2.8 to 5.0) with $1 \text{ mM NH}_4\text{F}$ showing enhanced reactivity in ice (Top) compared to liquid water (Bottom). (B) Fluoride concentration effects (0 to $1.0 \text{ mM NH}_4\text{F}$ added to pH 3.0 HF-buffered suspensions) in ice (blue) and liquid water (red). Total fluoride concentrations were determined by alkaline desorption. Dashed lines in panels A and B represent zero-order kinetic model fits. (C) Linear correlation demonstrates consistent 4.3-fold enhancement of iron dissolution in ice across all conditions ($R^2 = 0.99$). (D) Dissolution rates with NH_4F (total rates R_T in ice and liquid water, filled circles) vs. NH_4ClO_4 (proton-promoted rate R_H only, open circles) across pH 2.8 to 5.0, demonstrating ligand-specific enhancement. (E) Concentration dependence of total dissolution rates (R_T) at pH 3.0 (Left axis, closed circles), with corresponding fluoride surface loadings (Γ_F ; right axis, open circles) after 1-h equilibration. (F) Linear relationship between dissolution rates and fluoride surface loadings (Γ_F) in liquid water establishes mechanistic coupling ($R^2 = 0.91$, 95% CI shown). The slope yields $k_T = R_T/\Gamma_F = 7.29 \times 10^{-6}$ fluoride-complexed Fe per second (intercept is $R_T = -2.59 \times 10^{-5} \text{ } \mu\text{mol m}^{-2} \text{ s}^{-1}$). Negligible proton-promoted dissolution ($R_H \approx 0$; SI Appendix, Fig. S8 and Table S2), justifies $R_T = R_F + R_H \approx R_F$. Results demonstrate that enhanced dissolution in ice results from increased fluoride surface complexation, with dissolution rates directly correlating with surface ligand density across both phases.



was also required to account for adsorption at high fluoride concentrations and low pH (Fig. 3A). This aligns with previous work (21) demonstrating the ability of fluoride to undergo ligand exchange with $\equiv \text{Fe}_2\text{OH}$ sites. In contrast, the higher surface coordination number of OH in $\equiv \text{Fe}_3\text{OH}$ prevented any reaction.

Vibrational spectroscopy (Fig. 3E and F and SI Appendix, Fig. S5) substantiated this model by tracking fluoride surface complexes. We monitored O-H stretching band intensities ($3,661 \text{ cm}^{-1}$) of $\equiv \text{FeOH}^{-0.5}$ sites, which are most susceptible to ligand exchange forming $\equiv \text{FeF}^{-0.5}$ complexes (Eq. 1). Time-resolved experiments revealed faster $\equiv \text{FeOH}^{-0.5}$ site exchange in ice compared to liquid water (Fig. 3F). This finding aligned with higher iron dissolution rates and yields in ice. The results support $\equiv \text{FeF}^{-0.5}$ formation as the initial step leading to iron detachment from goethite in liquid-like microenvironments within ice. Although $\equiv \text{Fe}_2\text{OH}$ sites could not be resolved spectroscopically on goethite due to insufficient band resolution (21, 22), additional experiments with lepidocrocite nanoparticles, a γ - FeOOH polymorph with a face dominated by these sites, clearly showed preferential $\equiv \text{Fe}_2\text{OH}$ site exchange in ice at high fluoride concentrations (SI Appendix, Fig. S5). Accordingly, the model was calibrated to account for the coexistence of $\equiv \text{FeF}^{-0.5}$ and $\equiv \text{Fe}_2\text{F}$ complexes (Fig. 3G). In liquid

water, only $\equiv \text{FeF}^{-0.5}$ forms, whereas ice additionally promotes $\equiv \text{Fe}_2\text{F}$ formation at low pH and high loadings (Fig. 3A). This model provided a mechanistic basis for precursor complex formation that facilitated lattice Fe-O bond weakening and subsequent iron detachment (27), which from aqueous speciation modeling (SI Appendix, Fig. S6), should occur predominantly as the $\text{FeF}_3(\text{aq})$ complex. These predictions also exclude the possibility of $\text{FeF}_3(\text{s})$ precipitation (SI Appendix, Fig. S7 and Text).

Kinetic Modeling of Goethite Dissolution in Ice. Total dissolution rates comprise contributions from fluoride-promoted (R_F) and, under acidic conditions, proton-promoted (R_H) pathways: $R_T = R_F + R_H$. A kinetic model expressed R_F through fluoride surface speciation:

$$R_F = k_F(\Gamma_{\equiv \text{FeF}^{-0.5}} + \Gamma_{\equiv \text{Fe}_2\text{F}}), \quad [3]$$

where k_F is the rate constant (s^{-1}) and Γ represents surface loadings ($\mu\text{mol m}^{-2}$) of $\equiv \text{FeF}^{-0.5}$ and $\equiv \text{Fe}_2\text{F}$ predicted by surface complexation modeling. This formulation assumes equivalent reactivity for both surface species. This simplification is justified by the dominance of $\equiv \text{FeF}^{-0.5}$ under most conditions (>70% of surface fluoride; Fig. 3G) and the similar Fe-O bond-breaking steps required for detachment from either precursor. The linear relationship between fluoride surface loadings and dissolution rates

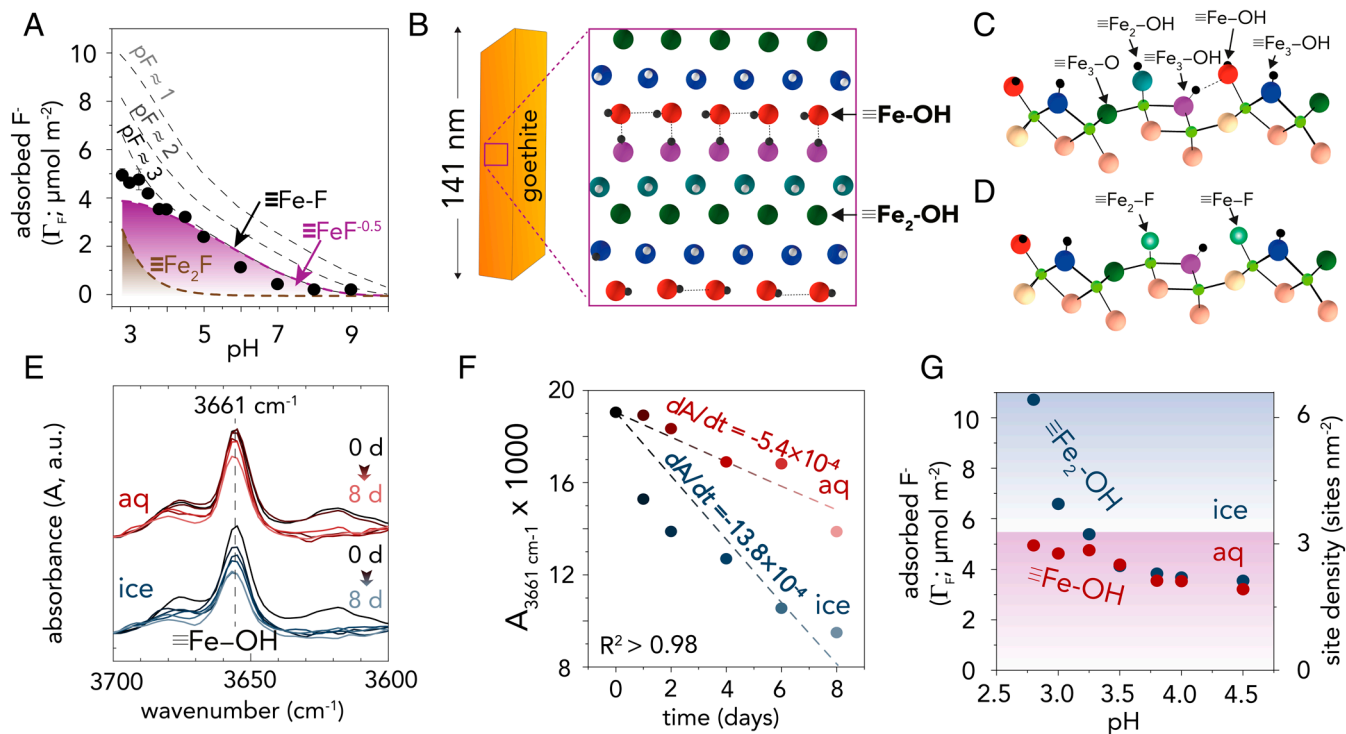


Fig. 3. Surface complexation controls fluoride-promoted dissolution through ligand exchange mechanisms. (A) pH-dependent fluoride surface loadings (Γ_F ; 1 mM NH_4F , 1 h, black circles) compared with surface complexation model predictions for varying fluoride concentrations (dashed lines). Shaded regions indicate dominant surface species. (B) Crystal structure of acicular goethite nanoparticle (average length of 141 nm from *SI Appendix*, Fig. S2) showing distribution of surface hydroxyl groups: singly coordinated $\equiv\text{Fe-OH}$ and doubly coordinated $\equiv\text{Fe}_2\text{-OH}$. (C) Surface structure before fluoride adsorption showing various hydroxyl coordination environments. (D) Surface structure after fluoride complexation showing formation of $\equiv\text{Fe-F}$ and $\equiv\text{Fe}_2\text{-F}$ surface complexes through ligand exchange. (E) Time-resolved vibrational spectra monitoring depletion of singly-coordinated surface hydroxyl groups ($3,661\text{ cm}^{-1}$ band) during 8-d dissolution in liquid water (red, Top) and ice (blue, Bottom). (F) Quantitative analysis of band absorbance (A) of $\equiv\text{Fe-OH}$ shows faster decay kinetics in ice ($dA/dt = -13.8 \times 10^{-4}\text{ d}^{-1}$) than in liquid water ($dA/dt = -5.4 \times 10^{-4}\text{ d}^{-1}$, $R^2 > 0.98$). (G) Predicted fluoride surface loadings (Γ_F) showing that enhanced complexation in ice correlates with available $\equiv\text{Fe-OH}$ and $\equiv\text{Fe}_2\text{-OH}$ site densities. Results demonstrate that surface complexation modeling accurately predicts fluoride adsorption and that enhanced dissolution corresponds to accelerated consumption of reactive surface sites, providing direct spectroscopic evidence for increased mineral-water interfacial reactivity during freezing.

in liquid water (Fig. 2F) yields an overall detachment rate constant $k_F = 7.29 \times 10^{-6}$ fluoride-complexed Fe per second.

We neglected contributions from R_H because iron detachment depends primarily on anion binding capability (Fig. 2D and *SI Appendix*, Table S2). Control experiments with ligands of contrasting iron-binding strengths confirmed this approach (Figs. 2D and 4A and *SI Appendix*, Fig. S8). Dissolution rates scaled with Fe(III)-ligand complexation strength (12, 28–30), while proton-promoted rates using perchlorate as a noncomplexing agent produced no measurable iron release (*SI Appendix*, Figs. S7 and S8 and Table S2). This justifies the approximation $R_T \approx R_F$.

These experiments also confirmed that enhanced dissolution in ice extends to other environmentally important anions, including chloride and sulfate. Dissolution rates scaled directly with the Gibbs free energy of Fe(III)-ligand complex formation (Fig. 4B), demonstrating thermodynamic control over ice-enhanced dissolution. The parallel slopes for ice and liquid water, offset by ~ 0.4 log unit, confirm consistent enhancement across all reactive ligands. Fluoride, the strongest iron-complexing ligand tested ($\log K_{\text{Fe-F}} = 13.6$), exhibited the highest dissolution rates in both liquid water and ice. Sulfate, with intermediate binding strength ($\log K_{\text{Fe-SO}_4} = 4.05$), showed moderate enhancement in ice, while chloride ($\log K_{\text{Fe-Cl}} = 2.13$) exhibited measurable but smaller effects. Perchlorate ($\log K_{\text{Fe-ClO}_4} = 0.62$), which forms only outer-sphere complexes with Fe(III), produced no measurable dissolution. This hierarchy, maintained in both liquid water and ice, matches the formation constants of their respective iron complexes, indicating

that freeze concentration amplifies existing ligand-mineral affinities rather than creating other reaction pathways. More broadly, the relationship between Gibbs free energy of complex formation and dissolution rates (Fig. 4B) provides a framework for assessing mineral reactivity in frozen environments. Although a rigorous linear free energy relationship would require normalization to surface ligand loadings, which is not possible for weakly binding anions (*SI Appendix*), the observed correlation under identical solution conditions (pH 3.0, 1 mM total ligand) is consistent with established correlations for organic ligand-promoted dissolution (15, 31).

Spatial Distribution of Goethite Dissolution Hot Spots in Ice.

To elucidate the environments in which dissolution rates were enhanced in ice, we mapped the spatial distribution of goethite nanoparticles and adsorbed fluoride using confocal Raman microscopy (Fig. 5 A–D and *SI Appendix*, Figs. S9 and S10). Lorentzian deconvolution of spectra over a $60 \times 60\ \mu\text{m}^2$ area in a frozen dilute goethite suspension resolved Fe-O vibrations from bulk goethite (386 cm^{-1}) and fluoride surface complexes (altered Fe-O bands at 400 and 418 cm^{-1}) (Fig. 5A) (27, 32). The Fe-F band components scaled directly with fluoride loadings (Fig. 5B).

Spatial mapping revealed that freezing transformed the initially dispersed goethite suspension into discrete micrometer-sized aggregates in ice (Fig. 5 C and D). This aligns with previous findings that freezing creates goethite aggregates with open nanopores that maintain reactivity comparable to dispersed nanoparticles

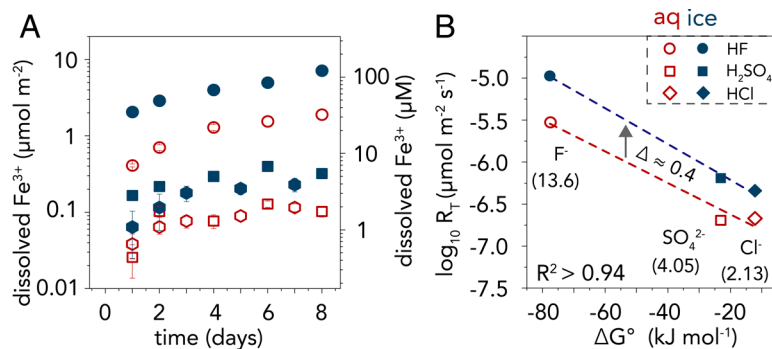


Fig. 4. Anion binding affinity controls goethite dissolution enhancement in ice. (A) Time-resolved iron release for different anions (HF, H₂SO₄, HCl) at pH 3.0, showing enhanced dissolution in ice (filled symbols) compared to liquid water (open symbols), with the strongest effects for fluoride. (B) Correlation between dissolution rates (R_T) and Gibbs free energy of complex formation (ΔG°) demonstrates thermodynamic control of ligand-promoted dissolution. Formation constants ($\log K$) for predominant 1:1 aqueous complexes are shown in parentheses. The linear relationship ($R^2 > 0.94$) indicates that stronger binding affinity drives faster dissolution rates in both ice and liquid water. The parallel slopes with a ~ 0.4 log unit offset ($\Delta \approx 0.4$) confirm consistent enhancement across ligand types. Conditions: 0.2 g L⁻¹ goethite at pH 3.0 in ice (-20°C) and liquid water (25°C). Results reveal that freeze concentration amplifies thermodynamically controlled dissolution processes.

(33, 34). Most significantly, the Fe-F component distribution (Fig. 5D) colocalized precisely with these goethite aggregates. Unlike high-salt systems where well-defined LIBs form distinct channels between ice crystals, the low ionic strength conditions examined here prevented formation of clearly delineated liquid boundaries. Instead, liquid water distributed as microscopic films and pockets associated with mineral aggregates. This spatial organization differs from our previous work with oxalate (11), which

formed concentrated LIBs at grain boundaries. The present study thus extends ice-enhanced dissolution to environmentally representative low-salt conditions while establishing a thermodynamic framework (Fig. 4B) that predicts dissolution enhancement for any ligand based on its iron binding affinity.

To quantify fluoride concentrations within liquid microenvironments during freezing, we used ¹H and ¹⁹F NMR on goethite-free solutions (Fig. 5 E–H and SI Appendix, Fig. S11). This builds upon

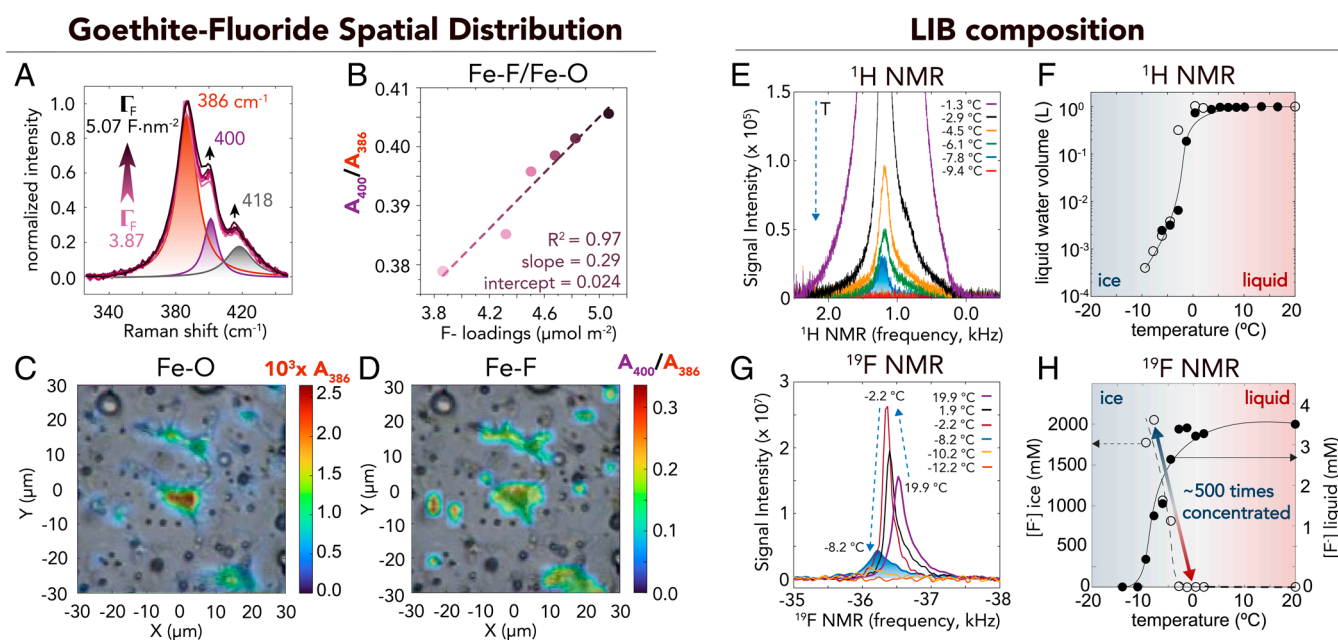


Fig. 5. Freeze concentration creates reactive liquid hot spots for enhanced mineral–ligand interactions. Spatial distribution by Raman microscopy (panels A–D) demonstrates colocalization of goethite nanoparticles and fluoride surface complexes, while NMR quantification (panels E–H) reveals residual liquid water and dissolved fluoride. (A) Representative Raman spectrum of goethite with fluoride surface complexes. Lorentzian deconvolution resolved bands from goethite (Fe–O vibrations at 330 to 450 cm⁻¹) and fluoride surface complexes (altered Fe–O vibrations at 400 and 418 cm⁻¹). (B) Linear correlation between Raman band area ratio (A_{400}/A_{386}) and fluoride surface loading provides a quantitative measure of surface complexation ($R^2 = 0.97$, slope = 0.29). (C and D) Confocal Raman mapping of frozen goethite suspension (1 g L⁻¹, 5 mM NH₄F, pH 2.5, -20°C) reveals spatial correlation between goethite aggregates (386 cm⁻¹ band area, panel C) and fluoride surface complexes (A_{400}/A_{386} ratio, panel D). Heat maps are overlaid on optical images of ice (50 \times magnification). (E) ¹H NMR spectra during progressive freezing to -9.4°C . (F) Temperature-dependent liquid water volume demonstrating progressive concentration from liquid (red region) to ice (blue region). Open and closed circles are from two separate experiments. (G) ¹⁹F NMR spectra quantifying fluoride in remaining liquid phases during freezing. (H) Estimated fluoride concentration within residual liquid water during progressive freezing, calculated from the fraction of unfrozen water and mass balance. As temperature decreases and ice fraction increases, fluoride concentrations in the diminishing liquid phase increase from 4 mM (liquid; Right axis, closed circles) to $\sim 2,000$ mM (ice; Left axis, open circles) just before complete freezing at -9.4°C . Lines in F and H are guidelines only. Results demonstrate that freeze concentration creates discrete microreaction zones where enhanced mineral–ligand interactions drive accelerated dissolution kinetics through formation of concentrated chemical microenvironments.

earlier work (35) showing the ability of ^1H NMR to probe the behavior of confined liquid water. Although goethite was excluded mainly to prevent magnetic interference from iron, these measurements provide essential baseline data for understanding the chemical environments where mineral dissolution occurs. Progressive freezing revealed systematic changes in both water and fluoride distribution. ^1H NMR spectra showed progressive liquid water exclusion, with only $\sim 0.2\%$ remaining at -9.4°C (Fig. 5E and F). Complete loss of the ^1H signal intensity below -9.4°C indicates this temperature as the practical lower limit for freeze concentration effects. Concurrently, ^{19}F NMR demonstrated that aqueous fluoride signal disappeared upon complete freezing (Fig. 5G). These complementary measurements enabled calculation of extreme chemical conditions within the remaining liquid phase. From the residual liquid water volume, we estimate that the LIB contained up to $\sim 2,000$ mM fluoride just before complete freezing (Fig. 5H), representing a ~ 500 -fold concentration enhancement over the initial 4 mM solution. This freeze concentration should also drive significant acidification, with pH shifting from the initial value of 3 to values potentially as low as 0.3.

Although NMR measurements on goethite-free solutions showed complete disappearance of the liquid water signal below -9.4°C , dissolution experiments at -20°C clearly demonstrated continued reactivity (Figs. 2 and 4). The observed reactivity strongly suggests that trace amounts of liquid-like water remained associated with goethite aggregates. Mineral surface interactions likely stabilized metastable liquid films, sustaining dissolution under the extreme chemical conditions established during freeze concentration. Additionally, the successful prediction of dissolution kinetics using surface complexation modeling suggests that the concentration factors we quantified are representative of the chemical environment experienced by mineral surfaces during freezing. Specifically, the measured concentration enhancement explains our prediction for activation of the $\equiv\text{Fe}_2\text{F}$ dissolution pathway only when fluoride concentrations are increased by freezing (Fig. 3G). These results demonstrate that freeze concentration creates geochemically distinct microenvironments that amplify mineral–water interactions even below the eutectic temperature (21, 36–42).

Discussion

Mineral–water interfacial processes control biogeochemical cycling across Earth's surface environments, regulating nutrient fluxes that influence ecosystem dynamics and human health (15–18, 43–45). As climate change accelerates ice loss in polar and alpine regions, understanding mineral reactivity in frozen systems becomes increasingly critical for predicting iron mobilization (3). Recent observations of enhanced Fe/Mn mineral reactivity in frozen media (46, 47) suggest that ice may function as an active geochemical medium rather than an inert storage phase.

This study demonstrates that ice acts as a geochemical reactor that alters mineral dissolution processes. Our mechanistic investigation reveals three key features of enhanced mineral dissolution in ice. First, freeze concentration expels dissolved species and mineral particles into residual liquid, creating discrete hot spots of elevated concentration. Second, enhanced surface complexation within these microenvironments accelerates ligand-promoted dissolution relative to ambient conditions. Third, interfacial reactivity persists even below the eutectic temperature, sustained by minute volumes of liquid-like water associated with mineral surfaces. Importantly, unlike our previous work with oxalate (11), where dissolution occurred in well-defined LIBs at grain boundaries, the low salt conditions examined here demonstrate that ice-enhanced

reactivity persists even when liquid water is distributed as microscopic films rather than distinct channels.

The thermodynamic control of dissolution by ligand binding affinity extends beyond fluoride to other environmentally important anions including sulfate and chloride. The consistent ~ 0.4 log unit enhancement across all reactive ligands demonstrates that ice-enhanced dissolution is a general phenomenon, with implications ranging from marine aerosol interactions to soil mineral transformations in permafrost regions. Although fluoride served here primarily as a mechanistic probe due to its strong iron-binding affinity, elevated fluoride concentrations do occur in cold environments through volcanic ash deposition and gas emissions (48, 49), weathering of fluorapatite in glacial sediments (50), and atmospheric deposition from industrial sources (51).

This framework proves particularly valuable for acidic systems where our experiments demonstrated maximum dissolution enhancement. Freeze concentration transforms moderately acidic solutions into highly acidic microenvironments, meaning dissolution enhancement can occur even when bulk conditions are only mildly acidic. Such starting conditions are widespread across diverse cold-region settings. At the soil–permafrost interface, active layer soils commonly exhibit pH 3.5 to 5.5 due to organic acid accumulation, with pH decreasing further during freezing (52, 53). Acid sulfate soils, formed when sulfide-bearing sediments are exposed by permafrost thaw, generate pH values as low as 2 to 3 through sulfide oxidation (54, 55). Sulfide-rich mine tailings and natural acid rock drainage maintain year-round acidity (pH 2 to 4) in contact with seasonal ice (56, 57). At the atmospheric scale, Arctic haze events deliver acidified aerosols (pH 2 to 4) to snow and ice surfaces, while volcanic emissions create locally extreme acidity in polar environments (58). The predictive capability of our thermodynamic framework becomes especially relevant as climate change increases freeze-thaw frequency and permafrost degradation, potentially amplifying mineral weathering rates and associated biogeochemical impacts.

These findings challenge the traditional view of ice as geochemically inert and reveal ice as an active participant in biogeochemical processes. By enhancing mineral dissolution, ice emerges as a driver of iron supply to polar ecosystems, with potential downstream effects on nutrient cycling and carbon dynamics. As warming temperatures reshape the extent and persistence of frozen landscapes worldwide, integrating ice-mediated chemistry into Earth system models will be critical for anticipating biogeochemical feedbacks to global change.

Materials and Methods

Dissolution Experiments. Dissolution experiments were performed using synthetic goethite nanoparticles ($81 \pm 4 \text{ m}^2 \text{ g}^{-1}$; *SI Appendix*) suspended in liquid water at 25°C and in polycrystalline ice at -20°C . Each sample contained 10 mL of goethite suspension (0.2 g L^{-1}) in 15 mL polyethylene tubes, diluted from concentrated stock (30 g L^{-1}) in Milli-Q water. Three experimental series involved i) various acids (HF , H_2SO_4 , HCl , HClO_4) at pH 3.0, ii) NH_4F concentration effects (0 to 1.0 mM) at pH 3.0, and iii) pH dependence (2.8 to 5.0) with 1.0 mM NH_4F or NH_4ClO_4 . Comparative experiments were also carried out with suspensions (0.2 g L^{-1}) of synthetic lepidocrocite ($82 \pm 2 \text{ m}^2 \text{ g}^{-1}$; *SI Appendix*) in 1.0 mM NH_4F at pH 3.0. Solution pH was controlled in all suspensions using 1 M solutions of the corresponding acids of the ligands under study.

All samples were degassed with $\text{N}_2(\text{g})$ for 30 min and sealed to prevent $\text{CO}_2(\text{g})$ contamination prior to the reactions. Liquid samples were agitated on an end-over-end rotator in a room at $25 \pm 1^\circ\text{C}$, while ice samples were prepared by rapid (~ 5 min) freezing in a precooled ethanol bath ($-20 \pm 0.01^\circ\text{C}$). The uniform color distribution in frozen samples indicated homogeneous particle dispersion in ice. To prevent photochemical reactions, all experiments were conducted in the dark. Time-resolved sampling involved thawing in lukewarm water ($\sim 40^\circ\text{C}$, 10 min),

after which particles were separated by centrifugation (8,000 rpm, 10 min), then filtration (0.2 μm). Melting time was insufficiently long to produce significantly more soluble iron (Fig. 2 A and B). Ferrous [Fe(II)] and total dissolved iron (Fe_{tot}) in the particle-free supernatants were analyzed by UV-Vis spectrophotometry (Cary-50, Varian) using the modified 1,10-phenanthroline method (59). These analyses were performed directly after centrifugation and filtration (SI Appendix). Reproducibility was $\sim 5\%$, with a detection limit of $\sim 1 \mu\text{M}$. No reductive dissolution was observed, as all measured dissolved Fe was only Fe(III).

Fluoride Adsorption Experiments and Surface Complexation Modeling. Fluoride adsorption was measured using mineral suspensions (0.2 g L^{-1} goethite or lepidocrocite) equilibrated with 1 mM NH_4F solutions at pH 2.8 to 9.0. After pH adjustment with 1 M HF and 1 h equilibration (cf. kinetic results of SI Appendix, Fig. S1), phases were separated by centrifugation. To account for additional fluoride introduced by HF at low pH, total fluoride was quantified by alkaline desorption (1 M NaOH, pH 12). Surface loading was calculated from the difference between total fluoride and equilibrium solution concentrations. All fluoride concentration measurements were performed at 25 $^\circ\text{C}$ using a fluoride-selective electrode (Orion) with TISAB IV ionic strength buffer. Predictions of fluoride adsorption on goethite were made using the multisite complexation model with PHREEQC (v.2.) (60). See SI Appendix for details.

Infrared Spectroscopy. Fourier-transform infrared (FTIR) spectroscopy monitored surface chemical changes following fluoride adsorption and mineral dissolution. Spectra were acquired using a Bruker Vertex 70/IV spectrometer with a DLATGS detector in the mid-infrared region (600 to 4,500 cm^{-1}) at 1 cm^{-1} spectral resolution.

Ligand exchange reactions were monitored through the vibrational signatures of surface OH groups. Spectra were acquired using $\text{N}_2(\text{g})$ -dried pastes of minerals reacted in the adsorption and dissolution experiments. FTIR spectra were acquired by attenuated total reflectance (Golden Gate, Specac) at 25 $^\circ\text{C}$, using a previously established protocol (25).

Raman Spectroscopy and Mapping. Raman microscopy was used to i) evaluate the influence of fluoride adsorption on goethite vibrations at ambient temperature, and ii) map the spatial distribution of goethite nanoparticles and fluoride ions in polycrystalline ice. Spectra were acquired in the 200 to 1,400 cm^{-1} range using a Renishaw InVia Qontor Raman spectrometer equipped with a 532 nm continuous-wave laser and 50 \times long working distance objective. Wet mineral pastes from fluoride adsorption experiments (pH 2.8 to 5.0) were analyzed first.

Fluoride loading-resolved spectra were linear baseline-corrected over 330 to 450 cm^{-1} and deconvoluted using a linear combination of Lorentzian functions.

Spatial analysis used $\sim 5 \mu\text{L}$ frozen droplets from goethite suspensions (1 g L^{-1}) pre-equilibrated with 5 mM NH_4F at pH 2.5 for 1 h. Droplets were placed on a cryogenic microscope stage (Linkam THMS600) and cooled from 25 to $-20 \text{ }^\circ\text{C}$ at 5 $^\circ\text{C min}^{-1}$ under a flow of $\text{N}_2(\text{g})$. Raman mapping covered $60 \times 60 \mu\text{m}^2$ areas at 3 μm resolution (SI Appendix, Fig. S10B). Maps were generated using the area of the 386 cm^{-1} (A_{386}) Lorentzian component for goethite and the area of the component of the fluoride complex at 400 cm^{-1} (A_{400}) normalized to that of goethite 386 cm^{-1} (A_{400}/A_{386}).

NMR. ^1H and ^{19}F NMR experiments were carried out on a Bruker 300 Avance III spectrometer operating at Larmor frequencies of 300.23 MHz for ^1H and 282.50 MHz for ^{19}F . A 4 mM NaF solution in a 5 mm NMR tube was initially frozen at $-80 \text{ }^\circ\text{C}$, then warmed to target temperatures. Methanol OH- CH_3 chemical shift separation dependence ($\Delta\nu$) was employed for temperature calibration (61). Measurements used a Diff50 PFG probe with 90 $^\circ$ pulse excitation and 20 s relaxation delays to satisfy quantitative NMR requirements for both ^1H and ^{19}F nuclei.

All NMR data are quantitative, with relaxation delays chosen for full magnetization recovery and a Curie law correction to account for temperature effects. Experiments were performed without locking procedures and using shimming values determined on liquid water at 20 $^\circ\text{C}$. Therefore, small shifts and line-shape modifications occurring with temperature were not relevant, but the integrated intensities provided reliable quantitative information from these measurements.

Data, Materials, and Software Availability. All data are available in the main text and SI Appendix.

ACKNOWLEDGMENTS. We acknowledge support from the Swedish Research Council (2020-04853 and 2024-04694), Formas (2022-01246), the Kempe Foundation (JCSMK 23-172), and the Carl-Tryggers Foundation (CTS 22:2326) to J.-F.B. and CNRS (IRP CHEMICY 2022-2027) to K.H. and J.-F.B. We also wish to thank the Vibrational Spectroscopy Core Facility, the Multipurpose Adaptive X-ray Scattering Platform, and the Umeå Centre for Electron Microscopy, all at Umeå University.

Author affiliations: ^aDepartment of Chemistry, Umeå University, Umeå SE-901 87, Sweden; and ^bÉcole Nationale Supérieure de Chimie de Rennes, CNRS, Institut des Sciences Chimiques de Rennes-UMR 6226, Université de Rennes, Rennes F-35000, France

1. W. J. Randel, E. J. Jensen, Physical processes in the tropical tropopause layer and their roles in a changing climate. *Nat. Geosci.* **6**, 169–176 (2013).
2. D. Mercier, "Climate change and the melting cryosphere" in *Spatial Impacts of Climate Change*, D. Mercier, Ed. (John Wiley & Sons, Ltd., 2021), pp. 21–41.
3. J. A. O'Donnell *et al.*, Metal mobilization from thawing permafrost to aquatic ecosystems is driving rusting of Arctic streams. *Commun. Earth Environ.* **5**, 268 (2024).
4. M. S. Patzner *et al.*, Iron mineral dissolution releases iron and associated organic carbon during permafrost thaw. *Nat. Commun.* **11**, 1–11 (2020).
5. L. J. A. Gerringa *et al.*, Iron from melting glaciers fuels the phytoplankton blooms in Amundsen Sea (Southern Ocean): Iron biogeochemistry. *Deep. Res. Part II Top. Stud. Oceanogr.* **71–76**, 16–31 (2012).
6. J. McCutcheon *et al.*, Mineral phosphorus drives glacier algal blooms on the Greenland Ice Sheet. *Nat. Commun.* **12**, 1–11 (2021).
7. M. Ramezanzadeh *et al.*, Effects of freeze-thaw cycles on methanogenic hydrocarbon degradation: Experiment and modeling. *Chemosphere* **325**, 138405 (2023).
8. D. Lannuzel *et al.*, The future of Arctic sea-ice biogeochemistry and ice-associated ecosystems. *Nat. Clim. Change* **10**, 983–992 (2020).
9. K. R. Miner *et al.*, Emergent biogeochemical risks from Arctic permafrost degradation. *Nat. Clim. Change* **11**, 809–819 (2021).
10. T. Bartels-Rausch *et al.*, Ice structures, patterns, and processes: A view across the icefields. *Rev. Mod. Phys.* **86**, 1205–1324 (2014).
11. A. P. Sebaaly, F. van Rijn, K. Hanna, J.-F. Boily, Ice as a kinetic and mechanistic driver of oxalate-promoted iron oxyhydroxide dissolution. *Proc. Natl. Acad. Sci. U.S.A.* **122**, 2017 (2025).
12. D. Jeong, K. Kim, D. W. Min, W. Choi, Freezing-enhanced dissolution of iron oxides: Effects of inorganic acid anions. *Environ. Sci. Technol.* **49**, 12816–12822 (2015).
13. K. Kim, W. Choi, M. R. Hoffmann, H. Il Yoon, B. K. Park, Photoreductive dissolution of iron oxides trapped in ice and its environmental implications. *Environ. Sci. Technol.* **44**, 4142–4148 (2010).
14. J. Du, K. Kim, D. W. Min, W. Choi, Freeze-thaw cycle-enhanced transformation of iodide to organoiodine compounds in the presence of natural organic matter and Fe(III). *Environ. Sci. Technol.* **56**, 1007–1016 (2022).
15. S. M. Kraemer, Iron oxide dissolution and solubility in the presence of siderophores. *Aquat. Sci.* **66**, 3–18 (2004).
16. J. J. Basinski *et al.*, Unraveling iron oxides as abiotic catalysts of organic phosphorus recycling in soil and sediment matrices. *Nat. Commun.* **15**, 5930 (2024).
17. H. Li, F. Santos, K. Butler, E. Herndon, A critical review on the multiple roles of manganese in stabilizing and destabilizing soil organic matter. *Environ. Sci. Technol.* **55**, 12136–12152 (2021).
18. O. S. Pokrovsky, J. Karlsson, R. Giesler, Freeze-thaw cycles of Arctic thaw ponds remove colloidal metals and generate low-molecular-weight organic matter. *Biogeochemistry* **137**, 321–336 (2018).
19. B. K. Biskaborn *et al.*, Permafrost is warming at a global scale. *Nat. Commun.* **10**, 1–11 (2019).
20. H. Liu, T. Chen, R. L. Frost, An overview of the role of goethite surfaces in the environment. *Chemosphere* **103**, 1–11 (2014).
21. T. Hiemstra, W. H. Van Riemsdijk, Fluoride adsorption on goethite in relation to different types of surface sites. *J. Colloid Interface Sci.* **225**, 94–104 (2000).
22. X. Ding, X. Song, J. F. Boily, Identification of fluoride and phosphate binding sites at FeOOH surfaces. *J. Phys. Chem. C* **116**, 21939–21947 (2012).
23. C. Noiriell, M. Oursin, D. Daval, Examination of crystal dissolution in 3D: A way to reconcile dissolution rates in the laboratory? *Geochim. Cosmochim. Acta* **273**, 1–25 (2020).
24. A. J. Anschutz, R. L. Penn, Reduction of crystalline iron(III) oxyhydroxides using hydroquinone: Influence of phase and particle size. *Geochem. Trans.* **6**, 60–66 (2005).
25. X. Song, J. F. Boily, Structural controls on OH site availability and reactivity at iron oxyhydroxide particle surfaces. *Phys. Chem. Chem. Phys.* **14**, 2579–2586 (2012).
26. C. Salazar-Camacho, M. Villalobos, Goethite surface reactivity: III. Unifying arsenate adsorption behavior through a variable crystal face - Site density model. *Geochim. Cosmochim. Acta* **74**, 2257–2280 (2010).
27. K. Klyukin, K. M. Rosso, V. Alexandrov, Iron dissolution from goethite (α -FeOOH) surfaces in water by ab initio enhanced free-energy simulations. *J. Phys. Chem. C* **122**, 16086–16091 (2018).
28. P. S. Sidhu, R. J. Gilkes, R. M. Cornell, A. M. Posner, J. P. Quirk, Dissolution of iron oxides and oxyhydroxides in hydrochloric and perchloric acids. *Clays Clay Miner.* **29**, 269–276 (1981).
29. T. Hiemstra, W. H. Van Riemsdijk, On the relationship between charge distribution, surface hydration, and the structure of the interface of metal hydroxides. *J. Colloid Interface Sci.* **301**, 1–18 (2006).
30. D. Peak, R. G. Ford, D. L. Sparks, An in situ ATR-FTIR investigation of sulfate bonding mechanisms on goethite. *J. Colloid Interface Sci.* **218**, 289–299 (1999).
31. G. Furrer, W. Stumm, B. Zinder, The coordination chemistry of weathering: II. Dissolution of Fe(III) oxides. *Geochim. Cosmochim. Acta* **50**, 1861–1869 (1986).

32. W. Stumm, R. Wollast, Coordination chemistry of weathering: Kinetics of the surface-controlled dissolution of oxide minerals. *Rev. Geophys.* **28**, 53–69 (1990).
33. L. Zhou, L. Lassabaterre, N. T. Luong, J.-F. Boily, K. Hanna, Mineral nanoparticle aggregation alters contaminant transport under flow. *Environ. Sci. Technol.* **57**, 2415–2422 (2023).
34. A. Hofmann *et al.*, Characterization of the pores in hydrous ferric oxide aggregates formed by freezing and thawing. *J. Colloid Interface Sci.* **271**, 163–173 (2004).
35. C. Richardson, Phase relationships in sea ice as a function of temperature. *J. Glaciol.* **17**, 507–519 (1976).
36. J. P. Nordin, D. J. Sullivan, B. L. Phillips, W. H. Casey, Mechanisms for fluoride-promoted dissolution of bayerite [β -Al(OH)₃(s)] and boehmite [γ -AlOOH]: ¹⁹F-NMR spectroscopy and aqueous surface chemistry. *Geochim. Cosmochim. Acta* **63**, 3513–3524 (1999).
37. V. Žutić, W. Stumm, Effect of organic acids and fluoride on the dissolution kinetics of hydrous alumina. A model study using the rotating disc electrode. *Geochim. Cosmochim. Acta* **48**, 1493–1503 (1984).
38. J. S. Geelhoed, T. Hiemstra, W. H. Van Riemsdijk, Phosphate and sulfate adsorption on goethite: Single anion and competitive adsorption. *Geochim. Cosmochim. Acta* **61**, 2389–2396 (1997).
39. M. L. Machesky, B. L. Bischoff, M. A. Anderson, Calorimetric investigation of anion adsorption onto goethite. *Environ. Sci. Technol.* **23**, 580–587 (1989).
40. R. P. J. J. Rietra, T. Hiemstra, W. H. Van Riemsdijk, Electrolyte anion affinity and its effect on oxyanion adsorption on goethite. *J. Colloid Interface Sci.* **229**, 199–206 (2000).
41. A. M. Grannas, A. R. Bausch, K. M. Mahanna, Enhanced aqueous photochemical reaction rates after freezing. *J. Phys. Chem. A* **111**, 11043–11049 (2007).
42. N. Takenaka, M. Tanaka, K. Okitsu, H. Bandow, Rise in the pH of an unfrozen solution in ice due to the presence of NaCl and promotion of decomposition of gallic acids owing to a change in the pH. *J. Phys. Chem. A* **110**, 10628–10632 (2006).
43. S. M. Fan, W. J. Moxim, H. Levy, Aeolian input of bioavailable iron to the ocean. *Geophys. Res. Lett.* **33**, 2–5 (2006).
44. E. Breitbarth *et al.*, Iron biogeochemistry across marine systems—Progress from the past decade. *Biogeosciences* **7**, 1075–1097 (2010).
45. G. Zhuang, Z. Yi, R. A. Duce, P. R. Brown, Link between iron and sulphur cycles suggested by detection of Fe(n) in remote marine aerosols. *Nature* **355**, 537–539 (1992).
46. K. Kim, H. Il Yoon, W. Choi, Enhanced dissolution of manganese oxide in ice compared to aqueous phase under illuminated and dark conditions. *Environ. Sci. Technol.* **46**, 13160–13166 (2012).
47. T. Chen *et al.*, Redox-driven formation of Mn(III) in ice. *Environ. Sci. Technol.* **58**, 15194–15201 (2024).
48. M. A. Armienta *et al.*, Fluoride in ash leachates: Environmental implications at Popocatepetl volcano, central Mexico. *Nat. Hazards Earth Syst. Sci.* **11**, 1949–1956 (2011).
49. A. Stefánsson *et al.*, Major impact of volcanic gases on the chemical composition of precipitation in Iceland during the 2014–2015 Holuhraun eruption. *J. Geophys. Res.* **122**, 1971–1982 (2017).
50. J. Zhou, H. Wang, C. A. Cravotta, Q. Dong, X. Xiang, Dissolution of fluorapatite by *Pseudomonas fluorescens* P35 resulting in fluorine release. *Geomicrobiol. J.* **34**, 421–433 (2017).
51. M. D. Cheng, Atmospheric chemistry of hydrogen fluoride. *J. Atmos. Chem.* **75**, 1–16 (2018).
52. A. Boman, S. Fröjdö, K. Backlund, M. E. Åström, Impact of isostatic land uplift and artificial drainage on oxidation of brackish-water sediments rich in metastable iron sulfide. *Geochim. Cosmochim. Acta* **74**, 1268–1281 (2010).
53. C. Yu *et al.*, Storage and distribution of organic carbon and nutrients in acidic soils developed on sulfidic sediments: The roles of reactive iron and macropores. *Environ. Sci. Technol.* **58**, 9200–9212 (2024).
54. E. Maudlet *et al.*, Tracing changes in base cation sources for Arctic tundra vegetation upon permafrost thaw. *Geoderma* **429**, 116277 (2023).
55. J. Zheng, E. C. Berns-Herrboldt, B. Gu, S. D. Wullschlegel, D. E. Graham, Quantifying pH buffering capacity in acidic, organic-rich Arctic soils: Measurable proxies and implications for soil carbon degradation. *Geoderma* **424**, 116003 (2022).
56. L. Parshley, Why are Alaska's rivers turning bright orange? Scientists have a theory. *Natl. Geogr. Mag.* (2025).
57. B. Dold, A. Aguilera, M. E. Cisternas, F. Bucchi, R. Amils, Sources for iron cycling in the Southern Ocean. *Environ. Sci. Technol.* **47**, 6129–6136 (2013).
58. H. O. T. Pye *et al.*, The acidity of atmospheric particles and clouds. *Atmos. Chem. Phys.* **20**, 4809–4888 (2020).
59. Z. Wang, H. Fu, L. Zhang, W. Song, J. Chen, Ligand-promoted photoreductive dissolution of goethite by atmospheric low-molecular dicarboxylates. *J. Phys. Chem. A* **121**, 1647–1656 (2017).
60. P. Lu, G. Zhang, J. Apps, C. Zhu, Comparison of thermodynamic data files for PHREEQC. *Earth Sci. Rev.* **225**, 103888 (2022).
61. A. L. Van Geet, Calibration of methanol nuclear magnetic resonance thermometer at low temperature. *Anal. Chem.* **42**, 679–680 (1970).